Research Square

Preprints are preliminary reports that have not undergone peer review.
They should not be considered conclusive, used to inform clinical practice,
or referenced by the media as validated information.

# Spontaneous Mineral-driven electrochemical synthesis of organic matter under Martian conditions

**Chenying Wang**

cwang11@carnegiescience.edu

Carnegie Institution of Washington https://orcid.org/0000-0003-4604-5290

**Andrew Steele**

Carnegie Institution for Science https://orcid.org/0000-0001-9643-2841

**Liane Benning**

GFZ, Helmholtz Centre for Geosciences https://orcid.org/0000-0001-9972-5578

**Sangyeon Lee**

Rensselaer Polytechnic Institute

**Richard Wirth**

GFZ Helmholtz Centre for Geosciences

**Anja Schreiber**

GFZ Helmholtz Centre for Geosciences

**Wencheng Lu**

Carnegie Institution of Washington, Earth and Planetary Laboratory

**Burkhard Kaulich**

Diamond Light Source

**Luis Hurtarte**

Diamond Light Source

**Jeffrey Paulo Perez**

GFZ Helmholtz Centre for Geosciences

**Anne Pommier**

Carnegie Institution of Washington, Earth and Planetary Laboratory

**George Cody**

Earth and Planets Laboratory, Carnegie Institution of Washington https://orcid.org/0000-0003-4176-3648

**Maria Jesus Herrero Perez**

Earth and Environmental Sciences, Rensselaer Polytechnic Institute;Rensselaer Astrobiology Research and Education (RARE) Centre

**Timothy A. Strobel**

Geophysical Laboratory, Carnegie Institution of Washington

**Karyn Rogers**

Earth and Environmental Sciences, Rensselaer Polytechnic Institute;Rensselaer Astrobiology Research and Education (RARE) Centre

---

**Article**

**Keywords:**

**Posted Date:** March 22nd, 2026

**DOI:** https://doi.org/10.21203/rs.3.rs-8911322/v1

**License:** This work is licensed under a Creative Commons Attribution 4.0 International License. Read Full License

**Additional Declarations:** There is **NO** Competing Interest.

---

# Abstract

Organic molecules preserved in Martian meteorites indicate that reduced carbon can form abiotically. Yet, the processes capable of generating and sustaining such material without biological or external energy inputs remain unresolved. Here, we demonstrate that a purely mineral-based system can spontaneously convert CO2 into complex organic matter through self-sustained electrochemical coupling. By embedding TiO2 and Fe3O4 nanoparticles within an amorphous SiO2 matrix, we construct a mineral assemblage that integrates an anodic phase, a cathodic phase and an electrolyte into a single electrochemical circuit. When immersed in CO2-bearing brine, this mineral junction drives directional electron transfer without applied voltage, illumination or heating. The system reduces CO2 to small oxygenated intermediates (e.g., formate, acetate) and subsequently converts them into aromatic-rich macromolecular carbon that accumulates at Fe-rich mineral interfaces. Nanoscale spectroscopic analyses show that these products closely resemble organic matter preserved in Martian meteorites. Unlike previous abiotic carbon synthesis studies that rely on isolated catalysts or external energy sources, this mineral assemblage sustains spontaneous, dark CO2 reduction driven solely by intrinsic mineral redox disequilibria. These findings identify mineral-driven geo-electrochemistry as a previously unrecognized pathway for abiotic carbon fixation and imply that similar processes could have operated on early Mars, early Earth and other water-bearing planetary bodies, while offering a conceptual framework for low-energy mineral-enabled carbon conversion.


# Introduction

Organic compounds indigenous to, and preserved within, Martian meteorites provide direct evidence that reduced carbon can form abiotically during aqueous alteration of planetary crusts.[1-6] These organics are consistently associated with Ti-Fe oxides, spinel-group minerals and amorphous silica formed during aqueous alteration[2,4,5], suggesting a mineralogical control on their synthesis. Proposed mechanisms include serpentinization[6], carbonation[6] and electrochemical reduction[5]. Electrochemical reduction of $CO_2$ was inferred from mineral and organic context and texture.

Fluid–rock interaction on Mars occurred predominantly within fractures and alteration veins[7,8], where redox contrasts between coexisting minerals would have been unavoidable[9]. Such environments are inherently electrochemical: minerals with different work functions and redox couples establish local potential gradients when immersed in electrolyte solutions[5]. Nanoscale intergrowths of Fe-rich and Ti-rich oxides embedded in silicate matrices, widely observed in Martian meteorites and alteration products[5], therefore resemble natural galvanic junctions capable of sustaining directional electron transfer during corrosion and weathering[10]. These mineral interfaces represent a plausible setting for abiotic carbon fixation, but their capacity to drive spontaneous carbon reduction has not been directly demonstrated.

Most experimental studies of abiotic carbon synthesis focus either on single “catalysts” usually in hydrothermal settings[11,12]. In contrast, mineral-driven electrochemical coupling offers a fundamentally different operating mode in which intrinsic potential gradients between dissimilar minerals i.e. galvanic processes, rather than temperature or light, provide the driving force for redox reactions[13-15]. While electrochemical reduction of $CO_2$ is a burgeoning research field for remediation of $CO_2$ from Earth’s atmosphere, the laboratory systems require external energy input, usually in the form of applied “over-potential (OP)”[16]. Therefore, bringing together observations of electrochemical reduction producing organics on Mars with the question of whether such mineral junctions can sustain carbon reduction under geochemically realistic conditions remains open.

Here, we construct a mineral assemblage that reproduces the textural and compositional relationships observed in Martian meteorites as discrete electrodes. By embedding $TiO_2$ and $Fe_3O_4$ nanoparticles within an amorphous $SiO_2$ matrix, we recreate Ti–Fe spinel–silicate interfaces formed during aqueous alteration of basaltic crust.[17] Experimental observation using both electrochemical, organic chemical, and nano-analytical techniques were then used to establish whether spontaneous galvanic coupling in aqueous brines, and the produced intrinsic electrochemical gradients could drive $CO_2$ reduction and organic synthesis without any external energy input.

## Results

# Spontaneous $CO_2$ reduction in a coupled mineral galvanic system

To evaluate whether mineral junctions can spontaneously drive $CO_2$ under Mars-like conditions, we constructed a galvanic system composed of $TiO_2{\cdot}aSiO_2$ and $Fe_3O_4{\cdot}aSiO_2$ electrodes immersed in $CO_2$-bearing brine. (Extended Data, Fig. 1) Analysis of Martian meteorites revealed the presence of amorphous silica throughout the organic-rich area, and for that reason, we designed the electrodes to encapsulate the oxide phases within a silica matrix[5,6]. Unlike previous abiotic $CO_2$ reduction studies that employ single catalysts activated by heat, light, or applied voltage, this configuration integrates distinct anodic and cathodic mineral phases. Details of the experimental methods are contained in the supplementary materials.

Post experimental analysis of the liquid phase by nuclear magnetic resonance spectroscopy (NMR, Fig. 1) and gas chromatography–mass spectrometry (GC-MS, Fig. 2) show that the coupled $TiO_2{\cdot}aSiO_2$–$Fe_3O_4{\cdot}aSiO_2$ contains a suite of soluble and mineral-associated organic compounds not present in the controls. Dominant products ($^1$H-NMR, Fig. 1A) include formate, acetate, acetone and methanol, with product distributions varying systematically with pH. Acidic and neutral conditions (Fig. 1A, data II, III. Extended Data Table. 1) favor small-oxygenated molecules, whereas alkaline conditions (Fig. 1A, data IV) promote the appearance of aromatic species. The emergence of aromatic resonances at 7.4–7.5 ppm in

$^{1}$H-NMR data (Fig. 1A curve IV) at high pH is accompanied by increased carbonate and carboxyl signals[18-21].

GC–MS (Fig. 2A) further detects formic acid, acetic acid and benzoic acid in reacted electrolytes, together with aromatic fragments associated with mineral-bound carbon. These compounds are absent from unreacted controls and from experiments conducted without $CO_2$. Consistent with GC–MS, $^{1}$H-NMR shows that after $CO_2$RR the coupled $TiO_2$·a$SiO_2$–$Fe_3O_4$·a$SiO_2$ system reproducibly yields acetate, acetone and methanol, whereas the corresponding control solutions contain at most trace acetate and no detectable acetone or methanol (Fig. 1A; Extended Data Table 1).

Isotopic labelling with $^{13}CO_2$ (Fig. 1B, 2B, Extended Data Fig. 5) demonstrates that carbon incorporated into formate, acetate and aromatic products derives from the supplied inorganic carbon source: $^{13}$C enrichment is observed in formate and aromatic carbon by $^{13}$C-NMR, and in both formate and acetate by GC–MS. The absence of resolved $^{13}$C-acetate resonances in solution-state $^{13}$C-NMR likely reflects differences in analytical sensitivity and/or spectral overlap under the present acquisition conditions. By contrast, acetone and methanol show no detectable $^{13}$C incorporation by either $^{13}$C-NMR or GC–MS, indicating that their carbon source cannot be unambiguously assigned to the introduced $^{13}CO_2$ in these experiments. Together, these data establish robust $CO_2$-to-organics conversion for formate, acetate and aromatic carbon, while constraining acetone and methanol to products whose isotopic provenance remains unresolved.

# Localization and structure of mineral-associated carbon

Building on Prior observation of aromatic macromolecular carbon (MMC) associated with magnetite and silica in Martian Meteorites[2,4,5,6], we investigated $Fe_3O_4$·a$SiO_2$ electrodes post-$CO_2$ reduction using similar techniques used to study the meteorites. Transmission electron microscopy (TEM, Figs. 3A-G, Extended Data Figs. 2-6) and synchrotron-based scanning transmission X-ray microscopy (STXM, Fig.3H) show that organic carbon accumulates preferentially at $Fe_3O_4$–$SiO_2$ interfaces after reaction (Fig. 3D, Extended Data Figs. 4,6). Non-reacted control samples display sharp magnetite–silica boundaries and lack localized carbon enrichment (Figs. 3B, H, Extended Data Fig.2). In contrast, reacted samples exhibit corrosion textures (Fig 3E and F) and interfacial carbon coatings that extend along oxide–silica boundaries (Fig 3C, D), indicating in situ formation and retention of carbon at mineral junctions (Figs. 3D, H, Extended Data Figs. 2,4,6).

High-resolution imaging and electron energy-loss spectroscopy (EELS, Fig 3C and D, Extended Data Fig. 6) identify amorphous carbon layers associated with Fe-rich domains. This spatial confinement demonstrates that carbon is generated and stabilized at magnetite–silica interfaces rather than being uniformly distributed throughout the electrolyte or mineral matrix.

The extent and morphology of interfacial carbon vary systematically with pH. At low pH (Extended Data Figs. 3, 6), magnetite remains embedded within amorphous silica and develops moderate porosity, with aromatic carbon retained at the oxide–silica boundary. At neutral pH (Extended Data Fig. 4), increased porosity and carbonate-rich amorphous phases emerge, consistent with partial dissolution and interfacial reorganization. Under alkaline conditions (Extended Data Fig. 5), extensive silica dissolution and magnetite corrosion lead to structural breakdown and partial release of organic products into solution.

C K-edge electron energy loss spectroscopy further distinguishes reacted samples from controls (Fig. 3H, Extended Data Table. 2)[29,30]. Control electrodes lack detectable aromatic signatures, whereas reacted electrodes display pronounced spectral features corresponding to aromatic, carboxyl and carbonate functional groups. These spectroscopic fingerprints[29,30] (Fig. 3H) closely resemble those reported for organic matter preserved in Martian meteorites (green trace Fig 3H), indicating that the experimentally generated carbon shares key chemical characteristics with Martian meteoritic organics.

Together, these observations establish that mineral interfaces act as both reactive sites and stabilizing hosts for newly formed organic matter. The preferential localization of aromatic-rich carbon at $Fe_3O_4$–$aSiO_2$ boundaries mirrors the association between amorphous silica and aromatic carbon observed in altered Martian meteorites.

# Electronic properties and band alignment of $TiO_2$·$aSiO_2$–$Fe_3O_4$·$aSiO_2$ pairs

The liquid and solid phase analyses confirm that the $TiO_2$·$aSiO_2$-$Fe_3O_4$·$aSiO_2$ acts as a galvanic pair system that can spontaneously reduce $CO_2$ to formate, acetate and aromatics across a wide pH range. To elucidate the origin of this activity and to confirm the reaction's validity and the intrinsic driving force behind spontaneous $CO_2$RR, we examined the electronic properties and band alignment of the two electrodes using Mott-Schottky and Cyclic Voltammetry analyses. Mott–Schottky analysis (Fig. 4A-C) shows that $TiO_2$·$aSiO_2$ behaves as an n-type semiconductor, whereas $Fe_3O_4$·$aSiO_2$ exhibits p-type character across the investigated pH range. Linear fits yield flat band potentials that define the relative positions of the semiconductor band edges and their systematic pH-dependent shifts. These data establish the energetic landscape of the Ti-Fe-silicate pair and constrain the alignment of its electronic states relative to solution redox couples and therefore confirm whether the two minerals could establish a natural potential difference when coupled. In simple terms, this analysis tells us whether the two minerals can naturally behave like a tiny battery when placed in water.

Independent open circuit potential measurements demonstrate that $Fe_3O_4$·$aSiO_2$ exhibits a lower equilibrium potential than $TiO_2$·$aSiO_2$ under identical electrolyte conditions, indicating that $Fe_3O_4$·$aSiO_2$ acts as the anodic phase and $TiO_2$·$aSiO_2$ as the cathodic phase when the two electrodes are electrically

coupled. Upon immersion in electrolyte, the p-type $Fe_3O_4$·a$SiO_2$ and n-type $TiO_2$·a$SiO_2$ therefore establish a mineral junction that supports spontaneous galvanic behavior, with $Fe^{2+}$ oxidation at the Fe-rich phase supplying electrons that are transferred to the Ti-rich phase, where they drive $CO_2$ reduction.[31]

The magnitude of the built-in potential and the resulting charge-transfer characteristics vary with pH. At low pH (Fig. 4A), large band offsets generate a strong internal electric field and pronounced galvanic coupling[31,33], favoring efficient electron flow between the two mineral phases. At neutral pH (Fig. 4B), reduced band separation enhances interfacial charge-transfer kinetics[34], consistent with changes in the organics produced in the liquid-phase analyses. Under alkaline conditions (Fig. 4C), the resulting galvanic potential, together with increased interfacial conductivity, enables multi-electron transfer and yields the highest activity[35], accompanied by enhanced formation of more structurally complex products.

Cyclic voltammetry recorded under galvanic coupling conditions (Fig. 4D-F) shows enhanced cathodic currents in $CO_2$-saturated brine relative to $N_2$-saturated electrolyte across the investigated pH range. The negative-going onset potentials in cathodic current under $CO_2$ indicate that the coupled mineral system generates sufficient intrinsic electrochemical bias to drive carbon reduction without external bias or illumination.

Notably, these electrochemical responses are not reproduced by either mineral phase alone under identical conditions (Extended Data Fig. 7). $TiO_2$·a$SiO_2$ in isolation produces only low yields of small-oxygenated products, whereas $Fe_3O_4$·a$SiO_2$ exhibits limited $CO_2$ reduction activity but efficiently transforms $CO_2$ reduction intermediates into more reduced and structurally complex organics. These observations indicate that the full reaction sequence requires both phases operating in an electrically coupled configuration.

# Coupled mineral behavior enables spontaneous carbon synthesis

The complementary electronic properties of the two minerals define the direction of electron flow and the sites of redox reactions. The conduction band of $TiO_2$·a$SiO_2$ lies at a more negative potential than the $CO_2$ redox couple, enabling thermodynamically favorable $CO_2$ reduction on $TiO_2$·a$SiO_2$ (Fig. 5).[36,37] Oxidation of $Fe^{2+}$ at the $Fe_3O_4$·a$SiO_2$ phase supplies electrons that are transferred to the $TiO_2$·a$SiO_2$ phase, where they drive the reduction of dissolved $CO_2$. The resulting products accumulate at mineral–silica interfaces and in solution, forming both small-oxygenated molecules and aromatic-rich carbon. This coupled electrochemical–mineralogical behavior provides a mechanistic link between mineral galvanic processes and abiotic organic synthesis under planetary conditions.

Control experiments using single-phase electrodes (supplementary doc 1.2) confirm that neither mineral alone can reproduce the full product suite. $TiO_2$·a$SiO_2$ reduces $CO_2$ only to small-oxygenated products (Extended Data Fig. 7A), whereas $Fe_3O_4$·$SiO_2$ shows limited $CO_2$ reduction activity but efficiently converts $CO_2$-reduction intermediates into more reduced and structurally complex organics, including aromatic species (Extended Data Fig. 7B, C). Together, the coupled mineral system functions as an integrated electrochemical reactor in which primary reduction and secondary upgrading occur within the same mineralogical framework.

# Discussion

This study establishes mineral-driven electrochemical coupling between two different minerals or even different phases of the same mineral as a previously unrecognized pathway for abiotic carbon fixation. This identifies galvanic mineral assemblages as natural electrochemical reactors that drive abiotic carbon fixation. By demonstrating that purely mineral assemblages can spontaneously convert $CO_2$ into complex organic matter without hydrothermal conditions or applied external energy input, we provide a mechanistic link between planetary mineralogy, electrochemistry and organic synthesis. In contrast to previous abiotic $CO_2$ reduction studies that rely on single catalysts,[41] our results (Fig. 5) show that a coupled mineral assemblage can function as a complete electrochemical circuit in which electron flow is generated internally by mineral redox disequilibria and directly coupled to $CO_2$ reduction. This identifies galvanic mineral assemblages as natural electrochemical reactors that drive abiotic carbon fixation.

The coupled $TiO_2$·a$SiO_2$–$Fe_3O_4$·a$SiO_2$ system exhibits clear functional differentiation between its two mineral components. $CO_2$ reduction occurs predominantly at the $TiO_2$·a$SiO_2$ surface, while $Fe_3O_4$·a$SiO_2$ functions as the electron source through $Fe^{2+}$ oxidation, generating small-oxygenated intermediates such as formate and acetate, together with additional oxygenated products including acetone. Whereas $Fe_3O_4$·a$SiO_2$ promotes secondary surface reactions that convert these intermediates into more reduced and structurally complex aromatic carbon. Single-electrode control experiments show that neither mineral alone can reproduce the full product suite, establishing that organic synthesis emerges from their coupled behavior rather than from the activity of either phase in isolation as in typically studied abiotic synthesis pathways.[42] Such division of labor is characteristic of electrochemical systems but has rarely been demonstrated in purely mineral assemblages and demonstrates that geo-electrochemical reactions supply energy to reactions in the environment.

The spontaneous operation of this system is explained by the complementary electronic properties of the two minerals. $TiO_2$·a$SiO_2$ consistently exhibits n-type character with a conduction band edge sufficiently negative to drive carbon reduction (Fig. 4,5). Their junction therefore establishes a built-in electric field that directs electrons from the Fe-rich phase toward the Ti-rich phase, generating potential differences that required for $CO_2$ reduction. This intrinsic driving force enables the coupled mineral system to operate spontaneously under ambient conditions, in contrast to single-phase electrodes that require large applied OPs to achieve comparable reactivity.[43]

The architecture of the $TiO_2$·a$SiO_2$–$Fe_3O_4$·a$SiO_2$ system mirrors key features of Martian alteration environments. Martian meteorites and rover observations document widespread co-occurrence of Fe–Ti oxides, spinel-group minerals and amorphous silica formed during aqueous alteration of basaltic crust. The exsolution lamellae seen in Martian spinels are capable of operating as nano-scale electrodes in a galvanic system, showing that when immersed in $CO_2$-bearing brines, such assemblages would naturally establish mineral junctions analogous to the anodic–cathodic pairing constructed here. Our design therefore represents a mineralogical analogue of fracture- and vein-hosted alteration textures, as well as areas of zonation within single minerals on Mars, in which redox disequilibria between coexisting phases could sustain electrochemical reactions during fluid–rock interaction.

Nanoscale imaging and spectroscopy (Fig. 3) show that organic carbon is spatially confined to magnetite–silica interfaces, linking carbon synthesis directly to mineral junctions. The emergence of aromatic carbon exclusively in reacted samples and its absence in controls demonstrate that these compounds are generated in situ rather than inherited from contamination. The close correspondence between experimentally produced aromatics and organic matter preserved in Martian meteorites suggests that similar mineral-driven electrochemical processes could have operated during aqueous alteration of Martian basalts.

The pH-dependent evolution of mineral textures (Fig. 1-3) further constrains the environmental conditions under which such processes can operate[44,45], with alkaline conditions favoring aromatic formation and indicating progressive carbon–carbon coupling and reduction. Moderate porosity and interfacial carbon retention at acidic and neutral pH favor the stabilization of organic products at oxide–silica boundaries[46,47], whereas strong alkalinity promotes mineral dissolution and the release of products into solution. These observations are consistent with scenarios in which carbon fixation occurs locally at mineral interfaces, but the resulting labile organic carbon can subsequently be redistributed by evolving fluid chemistry. The association of more refractory aromatic carbon with alteration textures in Martian meteorites is therefore consistent with episodic mineral-driven synthesis coupled to changing aqueous conditions.

More broadly, mineral-driven electrochemical synthesis provides a unifying framework linking corrosion, redox gradients, and organic carbon formation within planetary crusts. Similar Ti- and Fe-bearing assemblages occur in altered terrestrial basalts and are expected in the rocky interiors of icy ocean worlds[48,49], implying that this mechanism is not restricted to Mars. Mineral junctions capable of sustaining galvanic coupling may thus represent a general geochemical pathway for abiotic carbon fixation wherever igneous minerals interact with $CO_2$-bearing brines.

Beyond its planetary implications, this mechanism also redefines the conceptual landscape of electrochemical carbon reduction on Earth. Modern $CO_2$ reduction strategies are dominated by externally powered systems optimized for efficiency and selectivity[50]. In contrast, mineral-driven electrochemistry operates through intrinsic potential gradients generated by natural materials, offering a model for low-energy carbon conversion that does not require engineered catalysts or applied bias. Although such

systems are not optimized for industrial throughput, they demonstrate that carbon fixation can proceed under minimal energetic constraints when appropriate mineral assemblages are present.

Together, these results establish mineral-driven electrochemical coupling as a geochemically realistic and previously underappreciated mode of abiotic carbon synthesis. By directly linking semiconductor properties, nanoscale mineral textures, and organic product formation, this study provides a mechanistic explanation for the co-occurrence of Ti–Fe spinels, amorphous silica, and aromatic carbon in Martian meteorites and suggests that abiotic organic synthesis is an inherent consequence of fluid–rock interactions in redox-stratified environments on early Earth, Mars, and any other water-bearing planetary bodies.

## Materials and Methods

# Thin Film Electrode Synthesis

Magnetite-amorphous-silica thin-film electrodes ($Fe_3O_4$·a$SiO_2$) were synthesized by dispersing 150 mg of nano-magnetite powder (Fisher Scientific) in 20 mL of deionized water containing 500 µL of sodium silicate solution (“water glass”, Sigma-Aldrich). The suspension was sonicated for 15 min to achieve a uniform dispersion and then drop-cast onto fluorine-doped tin oxide (FTO) glass slides (conductive substrates, Sigma-Aldrich). Coated slides were dried and cured at 75 °C for 48 hrs to promote adhesion and formation of a stable amorphous silicate matrix. The resulting $Fe_3O_4$·a$SiO_2$ films consist of magnetite nanoparticles embedded within an a-$SiO_2$ framework and serve as the Fe-rich “spinel” endmember in the galvanic system. Titanium-amorphous-silica thin-film electrodes ($TiO_2$·a$SiO_2$) were prepared by dispersing 150 mg of $TiO_2$ nano powder (Sigma-Aldrich) in 20 mL of deionized water with 500 µL of sodium silicate solution, followed by 15 min sonication. The suspension was drop-cast onto FTO slides and treated identically (75 °C, 48 hrs) to yield $TiO_2$ nanoparticles encapsulated in an amorphous silica matrix. These electrodes represent the Ti-rich spinel domains.

# Analytical Techniques

Electrochemical reactions were carried out using the coupled $TiO_2$·a$SiO_2$–$Fe_3O_4$·a$SiO_2$ mineral system under $CO_2$-saturated aqueous conditions (Fig.S1). Product analysis and electrochemical measurements were performed on samples collected after reaction. All experiments were repeated independently four times with similar results (n = 4).

**Proton ($^1$H) and Carbon ($^{13}$C) - Nuclear Magnetic Resonance spectroscopy ($^1$H- and $^{13}$C- NMR):** Liquid-phase $CO_2$RR products were identified and quantified using $^1$H- and $^{13}$C-NMR. Spectra were acquired on a Bruker 600 MHz (14.1 T) AVIII NMR spectrometer under ambient conditions, using standard pulse sequences with water suppression, a 5 s relaxation delay, and no spinning. For each sample, 500 µL of electrolyte was mixed with 65 µL $D_2O$ (ACROS Organics) and 35 µL TMSP-$d_4$ (3-(trimethylsilyl) propionic

acid-$d_4$, Sigma-Aldrich) as an internal standard (58 µM for $^{1}$H-NMR; 20 mM for $^{13}$C-NMR). TMSP-$d_4$ was used for both chemical-shift referencing (0.00 ppm) and quantitative integration. (n=4)

**Headspace Solid-Phase Microextraction coupled with Gas Chromatography-Mass Spectrometry (HS-SPME-GC-MS):** Volatile and semi-volatile organics were analyzed by headspace solid-phase microextraction coupled with gas chromatography-mass spectrometry (HS-SPME-GC-MS) on an Agilent NW7590 GC-MS instrument using helium as the carrier gas and a 44 mins runtime. Electrolyte samples were acidified to pH ~1 with HCl, and 1 mL aliquots were transferred to 10 mL vials. AC-WR-95/PDMS fiber was exposed to the headspace at 80 °C for 1 h, then desorbed in the GC inlet at 260 °C for 10 min (n=4). Standard solutions of formic acid (7 mM), acetic acid (100 µM), phenol (100 µM), and saturated benzoic acid were run under identical conditions to determine retention times and identify corresponding peaks in $CO_2$RR samples (Fig.S7).

**Electrochemical characterization measurements (Gamry Interface 1000E Potentiostat/Galvanostat/ZRA Instrument):**

Electrochemical characterization was performed primarily in a three-electrode configuration using either $Fe_3O_4$·a$SiO_2$ or $TiO_2$·a$SiO_2$ as the working electrode (geometric area 1.0 cm²), a saturated calomel reference electrode (SCE), and a Platinum counter electrode. Cyclic voltammetry (CV) was carried out from 0.0 to -1.2 V vs SCE at a scan rate of 50 mV $s^{-1}$ with 1 mV step size (5 consecutive cycles, 2 s equilibration at the initial potential). Measurements were performed under $N_2$ and $CO_2$ at pH 2, 7, and 12 to determine $CO_2$RR onset potentials, open-circuit potentials (OCP), and current density enhancement under $CO_2$ relative to $N_2$ (n=4). Mott–Schottky (MS) was conducted with a 0.05 V potential step, 10 mV AC amplitude, and 3000 Hz ($Fe_3O_4$·a$SiO_2$) /100 Hz ($TiO_2$·a$SiO_2$) frequency, using an electrode area of 1 $cm^2$. For $Fe_3O_4$·a$SiO_2$/$TiO_2$·a$SiO_2$, Mott Schottky plots of $C^{-2}$ vs potential were used to extract flat-band potentials ($U_{FB}$) and carrier densities. (n=4) All potentials are reported versus SCE unless otherwise stated.

**Ultra-Violent-Via Spectroscopy for Band Gap and Electron Affinity Analysis:** Diffuse-reflectance UV-Vis spectra of $Fe_3O_4$·a$SiO_2$ and $TiO_2$·a$SiO_2$ films were acquired on a PerkinElmer Lambda 950 UV-Vis-NIR spectrophotometer with a 150 mm integrating sphere over 200-900 nm. Tauc plot analysis (Fig.S11) of Kubelka-Munk-transformed spectra yielded direct and indirect band gaps of $Fe_3O_4$·a$SiO_2$ and $TiO_2$·a$SiO_2$ (n=4).

**Transmission Electron Microscopy (TEM):** Focused ion beam (FIB) sections of $Fe_3O_4$·a$SiO_2$ electrodes were prepared and examined using a TECNAI F20 X-Twin TEM at 200 kV (Deutsches GeoForschungsZentrum, Potsdam), equipped with an EDAX EDS system, Gatan TRIDIEM imaging filter, and HAADF detector. Electron energy-loss spectroscopy (EELS) was performed in diffraction mode with 0.1 eV per pixel energy dispersion and 620 mm camera length to probe C K-edge features (e.g., ~285 and 290 eV). Spectra were analyzed using Digital Micrograph.

**Scanning Transmission X-ray Microscopy (STXM):** STXM measurements at the C 1s and N 1s absorption edges were carried out at Diamond Light Source (beamline I08, UK) on ultrathin FIB-prepared sections identified by TEM. Image stacks were collected with ~50 nm spatial resolution and 10 ms dwell time per pixel. Data were processed using MANTiS and aXis2000 to generate C K-edge XANES spectra and chemical-speciation maps.

# Declarations


### Acknowledgements

This work is supported by a NASA Astrobiology ICAR Program grant to K.L.R. and A.S., and by the Carnegie Institution of Washington. L.G.B., R.W. and A.S. acknowledge financial support from the Helmholtz Recruiting Initiative (I-044-16-01) awarded to L.G.B. J.P.H.P. acknowledges partial funding from the GFZ Discovery Fund (P-032-45-002). Beamtime at Diamond Light Source I08 was provided under proposals MG-36247 and MG-33333.


### Author contributions

C.W. designed the experiments, synthesized materials, conducted electrochemistry, NMR, GC–MS and microscopy analyses, and wrote the manuscript. A.S. supervised the project, TEM, EELS, STXM measurements and contributed to interpretation. L.G.B., R.W. and A.Sch. performed TEM and EELS. B.K. and L.C.C.H. conducted STXM measurements. S.L. and W.L. assisted with sample measurements. M.J.H.P., K.L.R., A.P., G.C. and T.A.S. contributed to planetary interpretation. All authors discussed results and contributed to manuscript editing.

### Competing interests

The authors declare no competing interests.

# References


1. Udry, A., Howarth, G. H., Herd, C. D. K., Day, J. M. D., Lapen, T. J. & Filiberto, J. What Martian meteorites reveal about the interior and surface of Mars. *J. Geophys. Res. Planets* **125**, e2020JE006523 (2020). https://doi.org/10.1029/2020JE006523
2. Schmitt-Kopplin, P., Matzka, M., Ruf, A., Menez, B., Chennaoui Aoudjehane, H., Harir, M., Lucio, M., Hertzog, J., Hertkorn, N., Gougeon, R. D., Hoffmann, V., Hinman, N. W., Ferrière, L., Greshake, A., Gabelica, Z., Trif, L. & Steele, A. Complex carbonaceous matter in Tissint martian meteorites give insights into the diversity of organic geochemistry on Mars. *Sci. Adv.* **9**, eadd6439 (2023). https://doi.org/10.1126/sciadv.add6439
3. Steele, A., McCubbin, F. M., Fries, M., Kater, L., Boctor, N. Z., Fogel, M. L., Conrad, P. G., Glamoclija, M., Spencer, M., Morrow, A. L., Hammond, M. R., Zare, R. N., Vicenzi, E. P., Siljeström, S., Bowden, R., Herd, C. D. K., Mysen, B. O., Shirey, S. B., Amundsen, H. E. F., Treiman, A. H., Bullock, E. S. & Jull, A. J.

T. A reduced organic carbon component in martian basalts. *Science* **337**, 212–215 (2012). https://doi.org/10.1126/science.1220715

4. Steele, A., McCubbin, F. M. & Fries, M. D. The provenance, formation, and implications of reduced carbon phases in Martian meteorites. *Meteorit. Planet. Sci.* **51** (2016). https://doi.org/10.1111/maps.12670
5. Steele, A., Benning, L. G., Wirth, R., Siljeström, S., Fries, M. D., Hauri, E., Conrad, P. G., Rogers, K., Eigenbrode, J., Schreiber, A., Needham, A., Wang, J. H., McCubbin, F. M., Kilcoyne, D. A. L. & Rodriguez Blanco, J. D. Organic synthesis on Mars by electrochemical reduction of $CO_2$. *Sci. Adv.* **4**, eaat5118 (2018). https://doi.org/10.1126/sciadv.aat5118
6. Steele, A., Benning, L. G., Wirth, R., Schreiber, A., Araki, T., McCubbin, F. M., Fries, M. D., Nittler, L. R., Wang, J., Hallis, L. J., Conrad, P. G., Conley, C., Vitale, S., O'Brien, A. C., Riggi, V. & Rogers, K. Organic synthesis associated with serpentinization and carbonation on early Mars. *Science* **375**, 172–177 (2022). https://doi.org/10.1126/science.abg7905
7. Cosgrove, J. W., Banham, S. G., Gupta, S. & Barnes, R. The origin of the fracture networks in the mudstones of Gale Crater Mars; their implications regarding the state of stress and fluid pressure during their formation and the depth to which they were buried. *J. Geophys. Res. Planets* **127**, e2022JE007313 (2022). https://doi.org/10.1029/2022JE007313
8. Oliver, N. H. S. & Bons, P. D. Mechanisms of fluid flow and fluid–rock interaction in fossil metamorphic hydrothermal systems inferred from vein–wallrock patterns, geometry and microstructure. *Geofluids* **2** (2002). https://doi.org/10.1046/j.1468-8123.2001.00013.x
9. Onstott, T. C., Ehlmann, B. L., Sapers, H., Coleman, M., Ivarsson, M., Marlow, J. J., Neubeck, A. & Niles, P. Paleo-rock-hosted life on Earth and the search on Mars: a review and strategy for exploration. *Astrobiology* **19**, 1230–1262 (2019). https://doi.org/10.1089/ast.2018.1960
10. Sharma, S., Roppel, R. D., Murphy, A. E., Beegle, L. W., Bhartia, R., Steele, A., Razzell Hollis, J., Siljeström, S., McCubbin, F. M., Asher, S. A., Abbey, W. J., Allwood, A. C., Berger, E. L., Bleefeld, B. L., Burton, A. S., Bykov, S. V., Cardarelli, E. L., Conrad, P. G., Corpolongo, A., Czaja, A. D., DeFlores, L. P., Edgett, K., Farley, K. A., Fornaro, T., Fox, A. C., Fries, M. D., Harker, D., Hickman-Lewis, K., Huggett, J., Imbeah, S., Jakubek, R. S., Kah, L. C., Lee, C., Liu, Y., Magee, A., Minitti, M., Moore, K. R., Pascuzzo, A., Rodriguez Sanchez-Vahamonde, C., Scheller, E. L., Shkolyar, S., Stack, K. M., Steadman, K., Tuite, M., Uckert, K., Werynski, A., Wiens, R. C., Williams, A. J., Winchell, K., Kennedy, M. R. & Yanchilina, A. Diverse organic-mineral associations in Jezero crater, Mars. *Nature* **619**, 724–732 (2023). https://doi.org/10.1038/s41586-023-06143-z
11. McCollom, T. M. & Seewald, J. S. Abiotic synthesis of organic compounds in deep-sea hydrothermal environments. *Chem. Rev.* **107**, 382–401 (2007). https://doi.org/10.1021/cr0503660
12. McCollom, T. M. & Seewald, J. S. Carbon isotope composition of organic compounds produced by abiotic synthesis under hydrothermal conditions. *Earth Planet. Sci. Lett.* **243**, 74–84 (2006). https://doi.org/10.1016/j.epsl.2006.01.027

13. Boily, J.-F. Molecular controls on complexation reactions and electrostatic potential development at mineral surfaces. *Rev. Mineral. Geochem.* **91A**, 105–147 (2025). https://doi.org/10.2138/rmg.2025.91A.04
14. Gao, X., Liu, K., Zhang, C., Cao, X., Sakamaki, T., Xie, X. & Li, X. Synergistic microbial and abiotic mechanisms of mineral-driven humic acid evolution for soil remediation. *J. Agric. Food Chem.* **73**, 31141–31151 (2025). https://doi.org/10.1021/acs.jafc.5c10844
15. Wan, H., Zhang, Z., Shi, Y., Hou, K., Liang, J., Wan, D. & Li, Y. Spatially confined catalytic interfaces driven by iron minerals for ultrafiltration membrane fouling control: fouling evolution and molecular dynamics simulation. *ACS ES&T Eng.* **5**, 4 (2025). https://doi.org/10.1021/acsestengg.4c00811
16. Liu, L. & Pant, D. Integrative electrochemical and biological catalysis for the mild and efficient utilization of renewable electricity and carbon resources. *Sustain. Energy Fuels* **8**, d3se00876b (2024). https://doi.org/10.1039/D3SE00876B
17. Toplis, M. J. & Carroll, M. R. An experimental study of the influence of oxygen fugacity on Fe–Ti oxide stability, phase relations, and mineral–melt equilibria in ferro-basaltic systems. *J. Petrol.* **36**, 1137–1170 (1995). https://doi.org/10.1093/petrology/36.5.1137
18. Fulmer, G. R., Miller, A. J. M., Sherden, N. H., Gottlieb, H. E., Nudelman, A., Stoltz, B. M., Bercaw, J. E. & Goldberg, K. I. NMR chemical shifts of trace impurities: common laboratory solvents, organics, and gases in deuterated solvents relevant to the organometallic chemist. *Organometallics* **29**, 2176–2179 (2010). https://doi.org/10.1021/om100106e
19. Danneels, D. & Anteunis, M. Influence of methyl substituents on the chemical shift of the ring protons in mono-, di- and trimethylcyclohexanes: a 300 MHz study of the $^{1}$H NMR spectrum of cis-1,3-dimethylcyclohexane. *Magn. Reson. Chem.***12**, 602–607 (1974). https://doi.org/10.1002/mrc.1270061202
20. Whaley, W. L., Okoso-Amaa, E. M., Womack, C. L., Vladimirova, A., Rogers, L. B., Risher, M. J. & Abraham, M. H. Summation solute hydrogen bonding acidity values for hydroxyl substituted flavones determined by NMR spectroscopy. *Nat. Prod. Commun.* **8**, 85–98 (2013). https://doi.org/10.1177/1934578X1300800121
21. Lomsadze, K., Domínguez Vega, E., Salgado, A., Crego, A. L., Scriba, G. K. E., Marina, M. L. & Chankvetadze, B. Separation of enantiomers of norephedrine by capillary electrophoresis using cyclodextrins as chiral selectors: comparative CE and NMR studies. *Electrophoresis* **33**, 1637–1647 (2012). https://doi.org/10.1002/elps.201200062
22. Yamamoto, Y. & Kanda, Z. The preparation and $^{13}$C-NMR spectra of alkoxymethyltriphenylphosphonium salts. *Bull. Chem. Soc. Jpn.* **53**, 3436–3438 (1980). https://doi.org/10.1246/bcsj.53.3436
23. O'Brien, C. P., Miao, R. K., Liu, S., Xu, Y., Lee, G., Robb, A., Huang, J. E., Xie, K., Bertens, K., Gabardo, C. M., Edwards, J. P., Dinh, C.-T., Sargent, E. H. & Sinton, D. Single pass $CO_2$ conversion exceeding 85% in the electrosynthesis of multicarbon products via local $CO_2$ regeneration. *ACS Energy Lett.* **6** (2021). https://doi.org/10.1021/acsenergylett.1c01122

24. Wang, N., Jiang, W., Yang, J., Feng, H., Zheng, Y., Wang, S., Li, B., Heng, J. Z. X., Ong, W. C., Tan, H. R., Zhang, Y.-W., Wang, D., Ye, E. & Li, Z. Contact-electro-catalytic $CO_2$ reduction from ambient air. *Nat. Commun.* **15**, 5913 (2024). https://doi.org/10.1038/s41467-024-50118-1
25. Johnson, R. L., Anderson, J. M., Shanks, B. H., Fang, X., Hong, M. & Schmidt-Rohr, K. Spectrally edited 2D $^{13}C$–$^{13}C$ NMR spectra without diagonal ridge for characterizing $^{13}C$-enriched low-temperature carbon materials. *J. Magn. Reson.***234**, 112–124 (2013). https://doi.org/10.1016/j.jmr.2013.06.006
26. Becker, J. & Wittmann, C. GC–MS-based $^{13}C$ metabolic flux analysis. *Methods Mol. Biol.* **1191**, 165–174 (2014). https://doi.org/10.1007/978-1-4939-1170-7_10
27. Martin, J.-M., Vacher, B., Ponsonnet, L. & Dupuis, V. Chemical bond mapping of carbon by image-spectrum EELS in the second derivative mode. *Ultramicroscopy* **65**, 229–238 (1996). https://doi.org/10.1016/S0304-3991(96)00071-X
28. Braun, A., Huggins, F. E., Shah, N., Chen, Y., Wirick, S., Mun, S. B., Jacobsen, C. & Huffman, G. P. Advantages of soft X-ray absorption over TEM-EELS for solid carbon studies––a comparative study on diesel soot with EELS and NEXAFS. *Carbon* **43**, 117–124 (2005). https://doi.org/10.1016/j.carbon.2004.08.029
29. Rothe, J., Plaschke, M. & Denecke, M. A. Scanning transmission X-ray microscopy as a speciation tool for natural organic molecules. *Radiochim. Acta* **92**, 711–715 (2004). https://doi.org/10.1524/ract.92.9.711.55004
30. Lehmann, J., Solomon, D., Brandes, J., Fleckenstein, H., Jacobson, C. & Thieme, J. Synchrotron-based near-edge X-ray spectroscopy of natural organic matter in soils and sediments. In *Biophysico-Chemical Processes Involving Natural Nonliving Organic Matter in Environmental Systems* (eds Senesi, N., Xing, B. & Huang, P. M.) 729–781 (Wiley, Hoboken, NJ, 2009). https://doi.org/10.1002/9780470494950.ch17
31. Verhagen, C. M., Jung, J.-I., Tikoo, S. M., Wittmann, A., Kring, D. A., Brachfeld, S., Wu, L., Burns, D. H. & Gulick, S. P. S. Significance of secondary Fe-oxide and Fe-sulfide minerals in upper peak ring suevite from the Chicxulub impact structure. *Minerals* **13**, 353 (2023). https://doi.org/10.3390/min13030353
32. Kroemer, H. Quasi-electric fields and band offsets: teaching electrons new tricks (Nobel lecture). *ChemPhysChem* **2**, 490–499 (2001). https://doi.org/10.1002/1439-7641(20010917)2:8/9
33. Tomlinson, W., Banou, S., Yu, C. C., Stojanovic, M. & Chowdhury, K. Comprehensive survey of galvanic coupling and alternative intra-body communication technologies. *IEEE Commun. Surv. Tutor.* **21**, 1146–1169 (2019). https://doi.org/10.1109/COMST.2018.2879643
34. Kumar, S., Ojha, K. & Ganguli, A. K. Interfacial charge transfer in photoelectrochemical processes. *Adv. Mater. Interfaces***4**, 1600981 (2017). https://doi.org/10.1002/admi.201600981
35. Li, X., Guan, X., Zhu, L., Li, H., Yin, X., Sun, S., Xu, H., Fan, Y., Li, P., Hu, L., Wu, Z., Pan, H., Wang, X., Cheng, Z., Jia, B. & Ma, T. Electron transfer in catalysis: from fundamentals to strategies. *Chem. Soc. Rev.* **54**, d4cs00600c (2025). https://doi.org/10.1039/D4CS00600C

36. Xu, Y. & Schoonen, M. A. A. The absolute energy positions of conduction and valence bands of selected semiconducting minerals. *Am. Mineral.* **85**, 543–556 (2000). https://doi.org/10.2138/am-2000-0416

37. Luo, W., Nie, X., Janik, M. J. & Asthagiri, A. Facet dependence of $CO_2$ reduction paths on Cu electrodes. *ACS Catal.* **6**(2016). https://doi.org/10.1021/acscatal.5b01967

38. Yu, F., Deng, K., Du, M., Wang, W., Liu, F. & Liang, D. Electrochemical $CO_2$ reduction: from catalysts to reactive thermodynamics and kinetics. *Carbon Capture Sci. Technol.* **6**, 100081 (2023). https://doi.org/10.1016/j.ccst.2022.100081

39. Lee, S., Wang, C. & Chakrapani, V. Spontaneous unassisted conversion of $CO_2$ to multicarbon liquid products on green rust mineral. Preprint at https://doi.org/10.26434/chemrxiv-2023-bch3f-v2 (2023).

40. Edholm, O., Nordlander, P., Chen, W., Ohlsson, P. I., Smith, M. L. & Paul, J. The effect of water on the Fe(III)/Fe(II) reduction potential of heme. *Biochem. Biophys. Res. Commun.* **268**, 683–687 (2000). https://doi.org/10.1006/bbrc.2000.2201

41. Ullah, N., Shah, S. S., Suliman, M. H., Ismail, F., Kaci, S., Amin, N. A. S. & Usman, M. Electrochemical $CO_2$ reduction: a review toward sustainable energy conversion and storage. *Energy Fuels* **39** (2025). https://doi.org/10.1021/acs.energyfuels.5c03761

42. Ahmad, Z. *Principles of Corrosion Engineering and Corrosion Control* (Butterworth-Heinemann, Oxford, 2006).

43. Cisternas, L. A., Lucay, F. A. & Botero, Y. A. Trends in modeling, design, and optimization of multiphase systems in minerals processing. *Minerals* **10**, 22 (2020). https://doi.org/10.3390/min10010022

44. Schieber, J., Bish, D., Coleman, M., Reed, M., Hausrath, E. M., Cosgrove, J., Gupta, S., Minitti, M. E., Edgett, K. S. & Malin, M. Encounters with an unearthly mudstone: understanding the first mudstone found on Mars. *Sedimentology* **64**, 367–386 (2017). https://doi.org/10.1111/sed.12318

45. Fox-Powell, M. G. & Cousins, C. R. Partitioning of crystalline and amorphous phases during freezing of simulated Enceladus ocean fluids. *J. Geophys. Res. Planets* **125**, e2020JE006628 (2020). https://doi.org/10.1029/2020JE006628

46. Ghosh, D., Das, S., Gahlot, V. K., Pulimi, M., Anand, S., Chandrasekaran, N., Rai, P. K. & Mukherjee, A. Nano-$SiO_2$ transport and retention in saturated porous medium: influence of pH, ionic strength, and natural organics. *J. Contam. Hydrol.* **248**, 104029 (2022). https://doi.org/10.1016/j.jconhyd.2022.104029

47. Bañuelos, J. L., Borguet, E., Brown, G. E. Jr, Cygan, R. T., DeYoreo, J. J., Dove, P. M., Gaigeot, M.-P., Geiger, F. M., Gibbs, J. M., Grassian, V. H., Ilgen, A. G., Jun, Y.-S., Kabengi, N., Katz, L., Kubicki, J. D., Lützenkirchen, J., Putnis, C. V., Remsing, R. C., Rosso, K. M., Rother, G., Sulpizi, M., Villalobos, M. & Zhang, H. Oxide- and silicate-water interfaces and their roles in technology and the environment. *Chem. Rev.* **123**, 6413–6544 (2023). https://doi.org/10.1021/acs.chemrev.2c00130

48. Zandanel, A., Hellmann, R., Truche, L., Roddatis, V., Mermoux, M., Choblet, G. & Tobie, G. Geologically rapid aqueous mineral alteration at subfreezing temperatures in icy worlds. *Nat. Astron.* **6**, 300–309 (2022). https://doi.org/10.1038/s41550-022-01613-2

49. Pereira, I., Bruand, E., Nicollet, C., Koga, K. T. & Vitale Brovarone, A. Ti-bearing minerals: from the ocean floor to subduction and back. *J. Petrol.* **64**, egad041 (2023). https://doi.org/10.1093/petrology/egad041

50. Lai, W., Qiao, Y., Zhang, J., Lin, Z. & Huang, H. Design strategies for markedly enhancing energy efficiency in the electrocatalytic $CO_2$ reduction reaction. *Energy Environ. Sci.* **15**, d2ee00472k (2022). https://doi.org/10.1039/D2EE00472K

# Figures

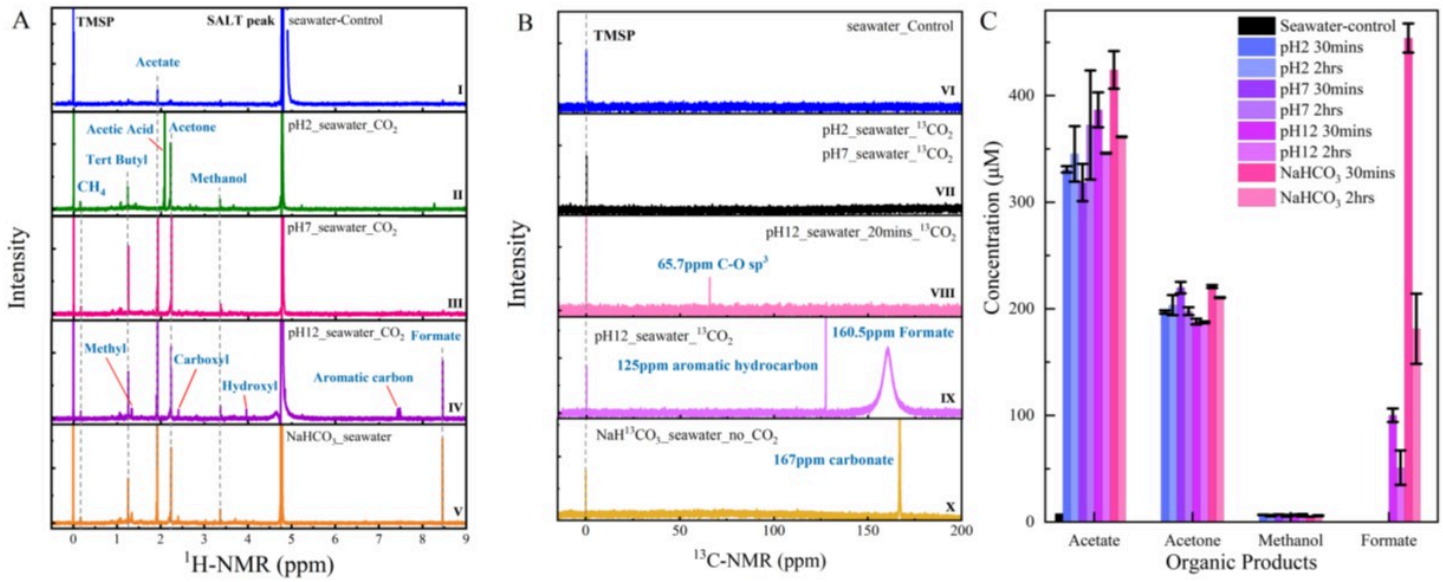



**Figure 1**

**Liquid-phase organic products generated during galvanic $CO_2$ reduction across pH conditions.** (A) $^1$H-NMR spectra of electrolyte solutions after $CO_2$RR, with TMSP (58 $\mu$M) used as an internal standard calibrated at 0.00 ppm. Peaks corresponding to acetate, acetone, methanol, formate and aromatic proton[18-21]. (B) $^{13}$C-NMR spectra highlighting carbon incorporation and chemical-shift evolution across pH values in $^{13}CO_2$ experiments; labelled formate and aromatic carbons appear at high pH.[22-25] (C) Quantified concentrations ($\mu$M) of major liquid-phase organics determined from $^1$H-NMR integration for $TiO_2$·a$SiO_2$–$Fe_3O_4$·a$SiO_2$ galvanic $CO_2$RR.

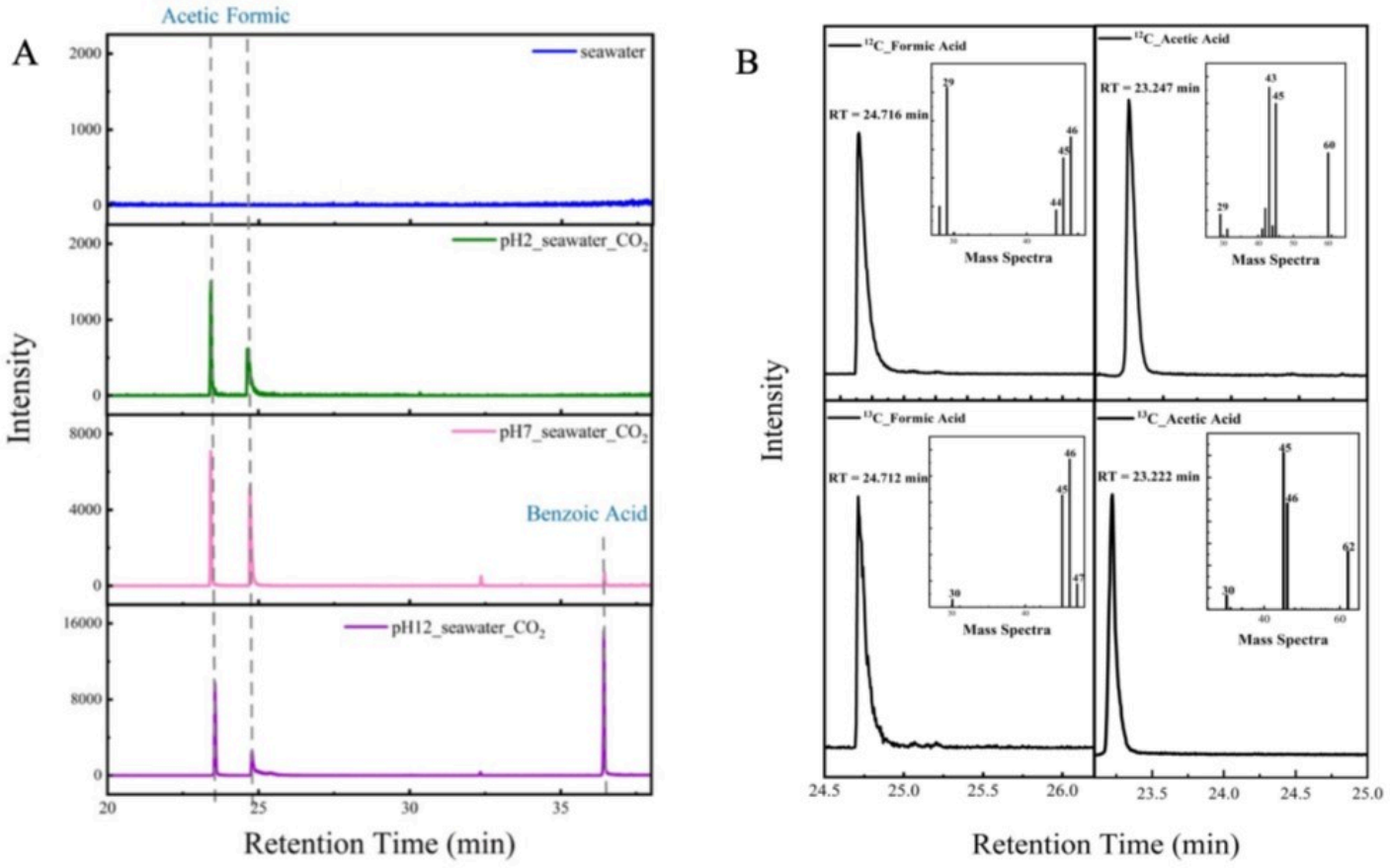



**Figure 2**

***GC–MS spectra of $CO_2$RR products under different pH conditions.*** *(A) GC–MS chromatograms of electrolyte solutions before and after 2 h of $CO_2$RR showing the distribution of acetic acid, formic acid and benzoic acid. (B) $^{13}$C-labelling experiments reveal slightly shorter retention times and a +1 amu shift per carbon in $^{13}$C-labelled acetic and formic acids, consistent with previous isotope studies.[26].*

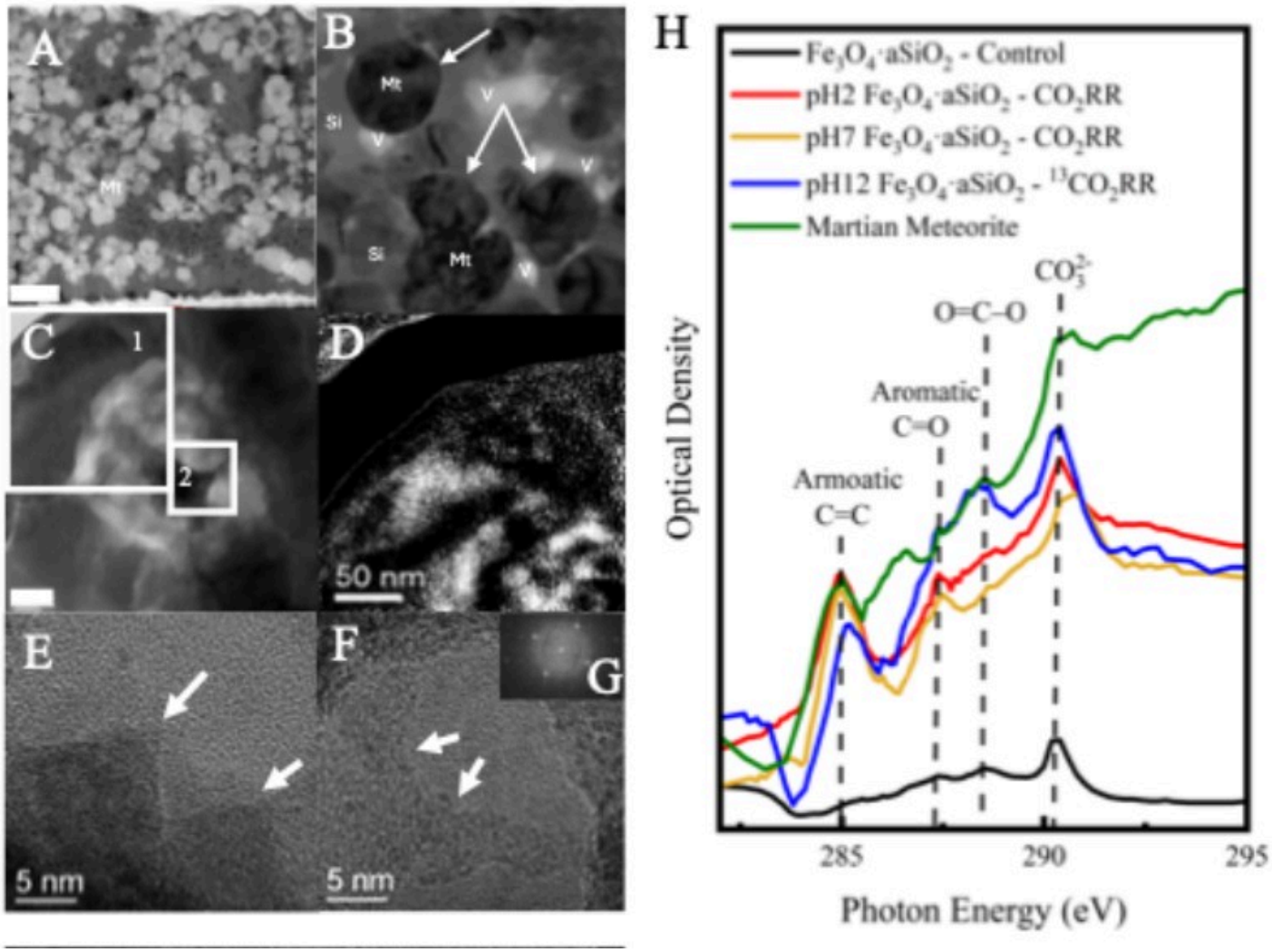



**Figure 3**

***TEM images of $Fe_3O_4$·aSi$O_2$ electrodes before (A-B) and after (C-F) $CO_2$RR.*** *A) Control sample (untreated electrode), displaying a well-preserved Magnetite (Mt) distribution within the silica matrix. B) Control sample at higher magnification: Magnetite (Mt) structure shows uncorroded sharp edges (white arrows) within a retained silica (Si) framework containing some void space (V). C) Image of a single magnetite cluster after $CO_2$RR, showing silica (light grey), and darker magnetite, within the center of the magnetite nanoparticles, Box 1 is an area mapped by EELS across the C1S edge (Extended Data Fig. 6D), Box 2, an area investigated by high-resolution imaging, shown in E and F (scale bar 5 nm). D) Carbon distribution (285.0 eV)[27,28] within the hollow center of the features in B and C. E) High-resolution image of Box 2, the magnetite silica interface reveals a triangular/dentate appearance to the edges of the magnetite nano-particles (white arrows), F) High-resolution image of amorphous silica is surrounded by the irregular surface of magnetite. G) Selected area diffraction from the area shown in F. H) STXM analysis reveals the formation and distribution of organic carbon species on the $Fe_3O_4$·aSi$O_2$ electrode before and after $CO_2$RR[29,30].*

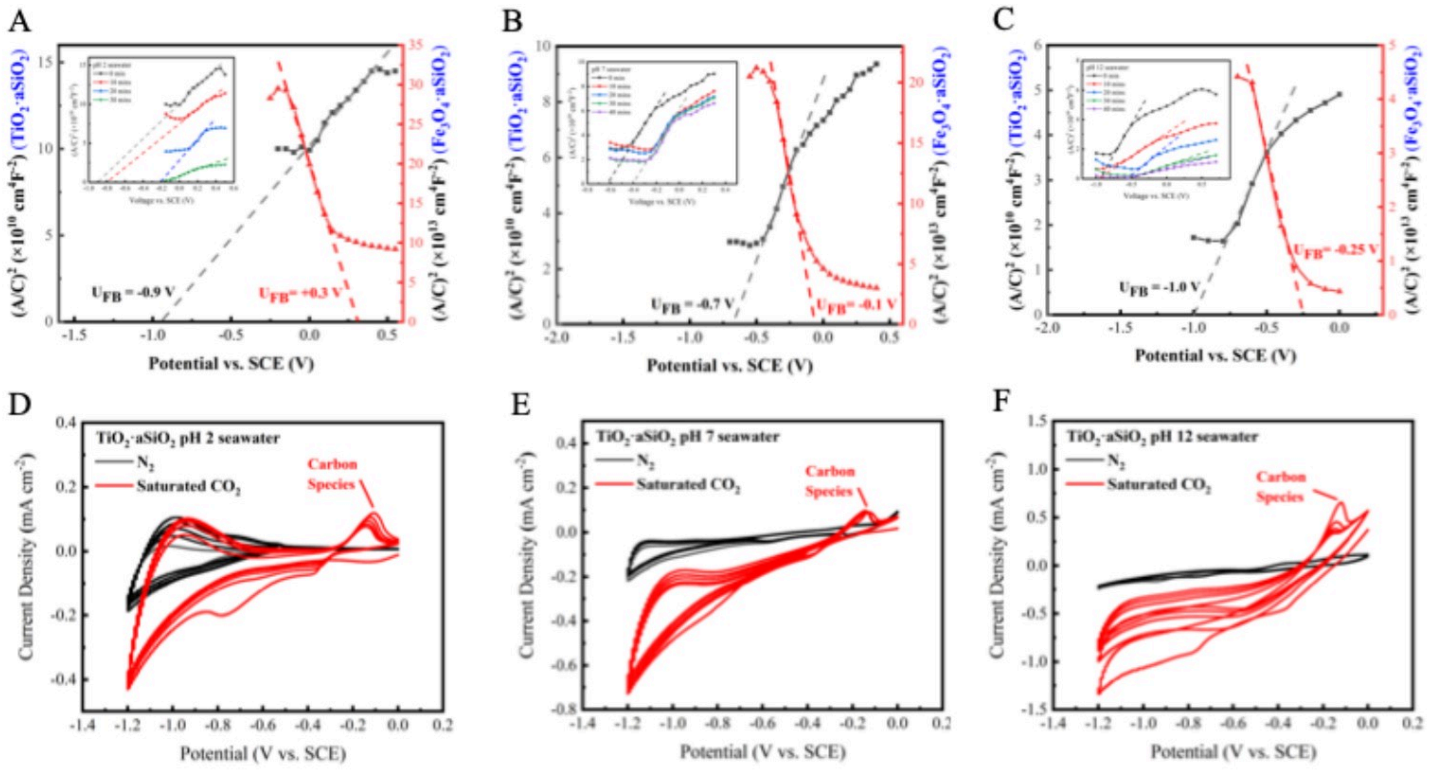



**Figure 4**

**pH-dependent band alignment and $CO_2$RR behavior of $TiO_2$·a$SiO_2$ and $Fe_3O_4$·a$SiO_2$ electrodes.** (A–C) Mott–Schottky (MS) plots of the capacitance ($C^{-2}$) versus potential (vs saturated calomel electrode, SCE) for $TiO_2$·a$SiO_2$ and $Fe_3O_4$·a$SiO_2$ electrodes in synthetic seawater at pH 2 (A), pH 7 (B) and pH 12 (C). (D–F) Cyclic voltammograms (CV) of the $TiO_2$·a$SiO_2$ at pH 2 (D), pH 7 (E) and pH 12 (F) in $N_2$-saturated (black) and $CO_2$-saturated (red) electrolyte.

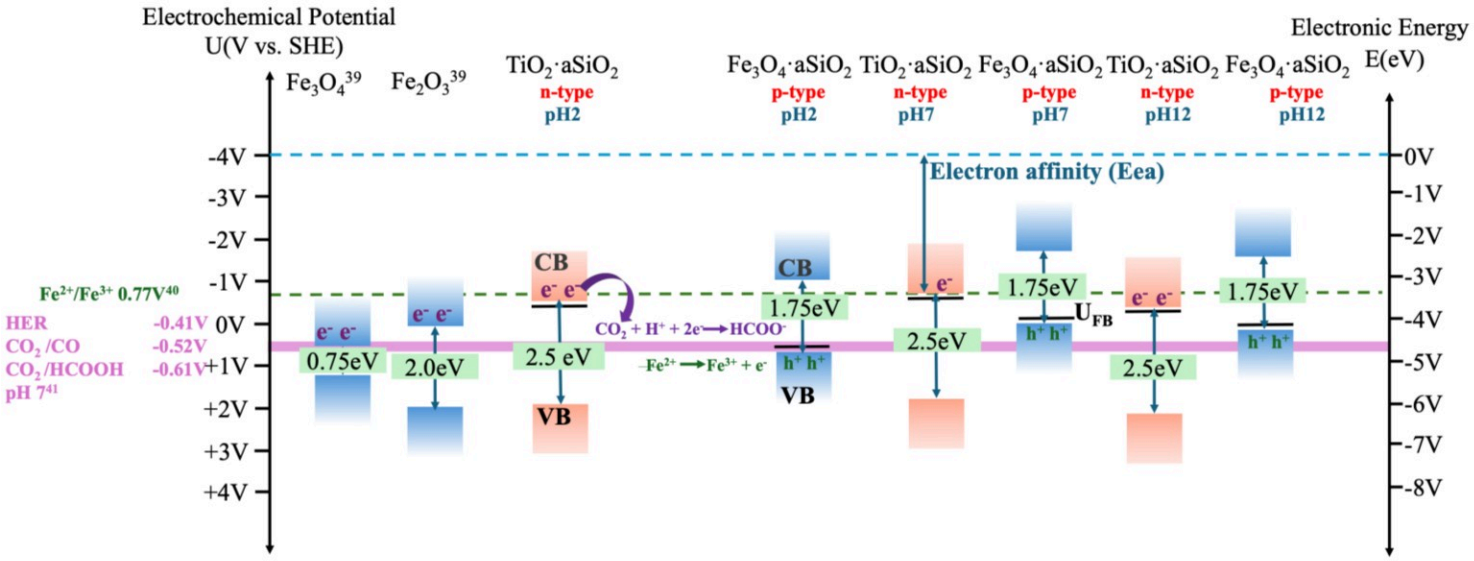



**Figure 5**

***pH-dependent band alignment and intrinsic driving force for galvanic $CO_2$ reduction on $TiO_2$·$aSiO_2$-$Fe_3O_4$·$aSiO_2$ pairs.*** *Schematic energy diagram showing the conduction band (CB) and valence band (VB) edges of $Fe_3O_4$, $Fe_2O_3$, $TiO_2$·$aSiO_2$ and $Fe_3O_4$·$aSiO_2$ at pH 2, 7 and 12. Energies are referenced both as electrochemical potentials (U vs. SHE, left axis) and electronic energies (eV, right axis). (p-type) $Fe_3O_4$·$aSiO_2$ and (n-type) $TiO_2$·$aSiO_2$; band-gap values are indicated inside each box. Horizontal dashed lines mark the $Fe^{3+}/Fe^{2+}$ redox couple and the pH-dependent $CO_2$/$CO_2$RR potentials. The built-in potential between $Fe_3O_4$·$aSiO_2$ and $TiO_2$·$aSiO_2$, together with their electron affinity ($E_{ea}$), drives electron flow from $Fe_3O_4$·$aSiO_2$ to $TiO_2$·$aSiO_2$ and enables spontaneous dark $CO_2$ reduction to organic products in the galvanic cell.*

## Supplementary Files

This is a list of supplementary files associated with this preprint. Click to download.

- extendeddatanature.docx